Modified momentum exchange method for fluid-particle interactions in the lattice Boltzmann method

Yang Hu and Decai Li*
School of Mechanical, Electronic and Control Engineering, Beijing Jiaotong University, Beijing, P.R. China 100044

Shi Shu
School of Mathematics and Computational Science, Xiangtan University, Xiangtan, P.R. China 411105

Xiaodong Niu
College of Engineering, Shantou University, Shantou, P.R. China 515063

(Received 16 September 2014; revised manuscript received 16 December 2014; published 4 March 2015)

In this paper, a modified momentum exchange method for fluid-particle interactions is proposed based on the finite-volume lattice Boltzmann method. The idea of the improvement is to remove the restriction that the boundary points must be set as the midpoints of the grid lines or the intersection of the grid lines with the solid boundaries. The particle surface is represented by a set of arc (area) elements, and the interior fluid is used which the geometric conservation law is naturally satisfied. The interactions between fluid and arc (area) elements of particle boundary are considered using the momentum exchange method, and the mass of the fluid particles which collide with an arc (area) element is obtained by means of numerical integration in the control volume. The fluid field is corrected with the help of the smooth kernel function. Moreover, a generalized explicit time marching scheme is introduced to resolve the motion of particle in the problems with the ratio of particle density to fluid density is close to or less than 1. Finally, some numerical case studies of particle sedimentation are carried out to validate the present method. The corresponding results have a good agreement with the previous literature, which strongly demonstrates the capability of the improved method.

DOI: 10.1103/PhysRevE.91.033301 PACS number(s): 47.11.−j, 47.55.Kf, 02.70.−c

I. INTRODUCTION

The fluid-particle interaction phenomenon exists widely in many fields ranging from chemical and environmental engineering processes to natural applications. However, our understanding of the interaction mechanism inside is very limited. With the help of the development of computer science, it is possible to investigate the complex fluid-particle interaction problem using computational fluid dynamics (CFD) methods. In recent years, the lattice Boltzmann method (LBM), which is derived from lattice automata, has received great attention due to its computational efficiency and convenience in programming. Compared with the conventional CFD methods, such as the arbitrary Lagrangian-Eulerian finite element method, LBM has unique advantages in treating fluid-particle interaction problems because the fluid is treated as particles. This feature enables the adoption of the momentum exchange method to calculate the coupling force without numerical integration or differentiation.

The pioneering work on the momentum exchange method in LBM was done by Ladd in 1994 [1,2]. In Ladd's model, the solid particle is treated as a thin shell, and the interior of the particle is assumed to be full of fluid. Similar to the exterior fluid, the density distribution function of the interior fluid is also updated after the collision or stream step. In other words, both exterior fluid and interior fluid are updated during the simulation in Ladd's method. So this model can be viewed as a shell model. The interaction between particle and fluid is implemented using the half-way bounce-back rule. The force act on the particle is computed by the momentum exchange method. The fluid field is updated automatically during implementing the bounce-back rule. The advantage of this method is that it can ensure the local conservation of mass and momentum. Compared with the point-particle models, this method can obtain more details of the flow field and has been adopted to simulate a variety of fluid-structure interaction problems successfully [1–3]. However, there exist two drawbacks in the shell model. One is that the particle boundary is represented by a series of the center points of the grid lines. This stepwise approximation would cause errors when the grid is coarse. Another drawback is that the computational procedure is not stable due to an explicit update of the particle velocity. When the ratio of particle density and fluid density is close to or less than 1, the numerical stability is more prominent. Since Ladd's pioneering work on the momentum exchange method in LBM, many subsequent researches have been conducted by many scholars. Aidun *et al.* proposed an improved momentum exchange method which involves only the exterior fluid [4]. In this model, a wide range of density ratio between particle and fluid can be simulated. However, this method involves complex local construction when the particle boundaries move. The geometric conservation law cannot satisfied either. So an impulse force technique which lack a detailed interpretation must be adopted to obtain correct particle dynamics [5,6]. Qi *et al.* developed another improved method by considering the advantages of models of Ladd and Aidun *et al.* [7]. Lorenz *et al.* analyzed the Galilean invariance in a conventional momentum exchange method. They proposed an approach

*dcli@bjtu.edu.cn

which can preserve Galilean invariance in relevant orders and improve the physical behavior of the particle-suspension system [8].

In order to simulate the particle motion with a real curve surface, many treatments have been proposed in recent years. Filippova *et al.* proposed a scheme to resolve the gas-particle flow with irregular shapes of the surfaces [9]. Later Mei *et al.* developed an accurate curved boundary method in the lattice Bhatnagar-Gross-Krook (BGK) model. It is worthwhile mentioning that this approach can work well when the relaxation time is close to 0.5 [10]. Bouzidi *et al.* analyzed the momentum transfer when dealing with curved boundaries in LBM [11]. Guo *et al.* proposed a boundary treatment for curved walls with well-behaved stability characteristics using the extrapolation method [12]. Lallemand *et al.* presented a technique to treat moving boundary problems by coupling the simple bounce-back scheme and interpolation methods [13]. Ginzburg and d'Humières provided a general framework (multireflection approach) for previously proposed boundary condition [14]. Later, Ginzburg extended the multireflection technique to treat arbitrarily shaped surfaces [15]. Wen *et al.* developed a lattice type-dependent momentum-exchange method to compute the hydrodynamics force for moving boundaries. This method can preserve the advantages of conventional method [5]. Chen *et al.* considered the initial momentum of the net mass transfer at each time step and proposed another corrected momentum exchange method [6]. Moreover, for the sake of ensuring the stability of the particle motion algorithm, an implicit update scheme had been proposed by Lowe *et al.* [16]. However, the computational cost increases although the stability restriction is relaxed. The idea of momentum exchange is also extended to construct the immersed boundary scheme. A key formula is dimensionally inconsistent in the initial studies [17–19], and the correct form can be found in Ref. [20].

The main purpose of this paper is to construct a simple, efficient, robust, and easy implementing momentum exchange method. The lattice BGK model based on the view of finite volume method is used to solve the fluid flow fields. Meanwhile, in Ladd's initial method, both the interior and exterior fluids are used when treating the solid boundaries. Different from the previous momentum exchange methods and interpolation-based curved boundary treatment methods, the marker points which represent the curved boundary can be collocated more freely. With the help of the control volume method, the momentum change of the arc(area) element in the particle surface can be computed. Then the force acting on the fluid nodes is obtained using the kernel function, which is commonly employed in many particle simulation methods. Since we do not need to distinguish the exterior fluid nodes and interior fluid nodes in the present method, the coding implementation is very easy. Moreover, based on the work of Feng and Michaelides [21], we propose a time stepping scheme which can treat the problems when the ratio of particle density and fluid density is close to or less than 1. Some numerical examples, including single-circular-particle sedimentation, single-elliptical-particle sedimentation, and two-particle sedimentation, are simulated to verify the present scheme.

II. NUMERICAL METHODOLOGY

A. Lattice Boltzmann method

The LBM can be regarded as an alternative technique of the Navier-Stokes fluid field solver, and it is a very popular kinetic scheme in recent years. In this paper, the lattice Boltzmann model based on view of finite-volume method is used. In other words, the density distribution function which is discussed in the present study is the local volume average value. The evolution equations of lattice Boltzmann model with an external force term are written as follows:

$$f_\alpha(\mathbf{x}+\mathbf{e}_\alpha\Delta t, t+\Delta t) - f_\alpha(\mathbf{x},t) = -\frac{1}{\tau}\left[f_\alpha(\mathbf{x},t) - f_\alpha^{\mathrm{eq}}(\mathbf{x},t)\right] + F_\alpha\Delta t, \tag{1}$$

where $f_\alpha(\mathbf{x},t)$ is the density distribution function for the discrete velocity $\mathbf{e}_\alpha$, Δt is the time step, and $f_\alpha^{\mathrm{eq}}(\mathbf{x},t)$ is the local equilibrium density distribution function, which can be computed by

$$f_\alpha^{\mathrm{eq}}(\mathbf{x},t) = \omega_\alpha\rho\left[1 + \frac{\mathbf{e}_\alpha\cdot\mathbf{u}}{c_s^2} + \frac{(\mathbf{e}_\alpha\cdot\mathbf{u})^2}{2c_s^4} - \frac{\mathbf{u}^2}{2c_s^2}\right], \tag{2}$$

where c_s is the lattice sound speed and ω_α is the weight coefficient, which depends on the lattice velocity model. τ is the dimensionless relaxation time of velocity field, which can be obtained as follows:

$$\tau = \frac{\nu}{c_s^2\Delta t} + 0.5, \tag{3}$$

where ν is the kinematic viscosity.

In this study, three lattice models (D2Q9, D3Q15, D3Q19) are used, and the velocity sets are defined as

$$\mathbf{e}_\alpha = \begin{cases} (0,0), & \alpha = 0 \\ \left(\cos\left[(\alpha-1)\frac{\pi}{2}\right], \sin\left[(\alpha-1)\frac{\pi}{2}\right]\right)c, & \alpha = 1\sim 4 \\ \left(\cos\left[(2\alpha-1)\frac{\pi}{4}\right], \sin\left[(2\alpha-1)\frac{\pi}{4}\right]\right)c, & \alpha = 5\sim 8 \end{cases} \tag{4}$$

$$\mathbf{e}_\alpha = \begin{cases} (0,0), & \alpha = 0 \\ (\pm1,0,0)c,(0,\pm1,0)c,(0,0,\pm1)c, & \alpha = 1\sim 6 \\ (\pm1,\pm1,\pm1)c, & \alpha = 7\sim 14, \end{cases} \tag{5}$$

and

$$\mathbf{e}_\alpha = \begin{cases} (0,0), & \alpha = 0 \\ (\pm1,0,0)c,(0,\pm1,0)c,(0,0,\pm1)c, & \alpha = 1\sim 6 \\ (\pm1,\pm1,0)c,(0,\pm1,\pm1)c,(\pm1,0,\pm1)c, & \alpha = 7\sim 18, \end{cases} \tag{6}$$

where $c = \Delta x/\Delta t$, Δx is the lattice spacing. Further, $c = \sqrt{3}c_s$. In the case of $\Delta x = \Delta t$, c is taken as 1. The corresponding weight coefficients are given as

$$\omega_\alpha = \begin{cases} \frac{4}{9}, & \alpha = 0 \\ \frac{1}{9}, & \alpha = 1 \sim 4 \\ \frac{1}{36}, & \alpha = 5 \sim 8, \end{cases} \tag{7}$$

$$\omega_\alpha = \begin{cases} \frac{2}{9}, & \alpha = 0 \\ \frac{1}{9}, & \alpha = 1 \sim 6 \\ \frac{1}{72}, & \alpha = 7 \sim 14, \end{cases} \tag{8}$$

and

$$\omega_\alpha = \begin{cases} \frac{1}{3}, & \alpha = 0 \\ \frac{1}{18}, & \alpha = 1 \sim 6 \\ \frac{1}{36}, & \alpha = 7 \sim 18. \end{cases} \tag{9}$$

The force term F_α is obtained using the Guo-Zheng-Shi model [22]:

$$F_\alpha = \left(1 - \frac{1}{2\tau}\right)\omega_\alpha\left(\frac{\mathbf{e}_\alpha - \mathbf{u}}{c_s^2} + \frac{\mathbf{e}_\alpha \cdot \mathbf{u}}{c_s^4}\mathbf{e}_\alpha\right) \cdot \mathbf{f}. \tag{10}$$

The macro density and velocity are given by

$$\rho = \sum_\alpha f_\alpha, \tag{11}$$

$$\mathbf{u} = \left(\sum_\alpha \mathbf{e}_\alpha f_\alpha + 0.5\mathbf{f}\Delta t\right) \Big/ \rho. \tag{12}$$

B. Modified momentum exchange method

In the present method, the boundary of the solid particle is represented by a series of movable control arc (area) elements, and the maker points are located in the center of the control arc (area) element. This technique has been widely used in immersed boundary method and front tracking method [23,24]. Different from the conventional momentum exchange method based on the midway bounce-back boundary condition [1–3], the maker points are located at the real curved boundary in the present method. This treatment can avoid some discrete boundary errors in the original method. Compared with the momentum exchange method based on curved boundary conditions, the number of mark points is conserved. In Ref. [25], Seo and Mittal identify the primary cause of spurious oscillations in the sharp-interface immersed boundary method to be a lack of the geometric conservation law near the boundary. Although the momentum exchange method based on curved boundary conditions is different from the sharp-interface method, when dealing with the moving boundary problems, the number of points which represent the boundary is variable in the two methods. So violation of the geometric conservation law may be one of reasons which lead to the force oscillation.

Now we consider the interaction between the arc (area) element and the fluid. In Fig. 1 it can be seen that the fluid particles which are located in the interior domain and exterior domain with different discrete velocity will collide with the solid boundary element. As shown in Fig. 2, in the time interval $[t_{n-\frac{1}{2}}, t_{n+\frac{1}{2}}] = [(n-\frac{1}{2})\Delta t, (n+\frac{1}{2})\Delta t]$, the fluid

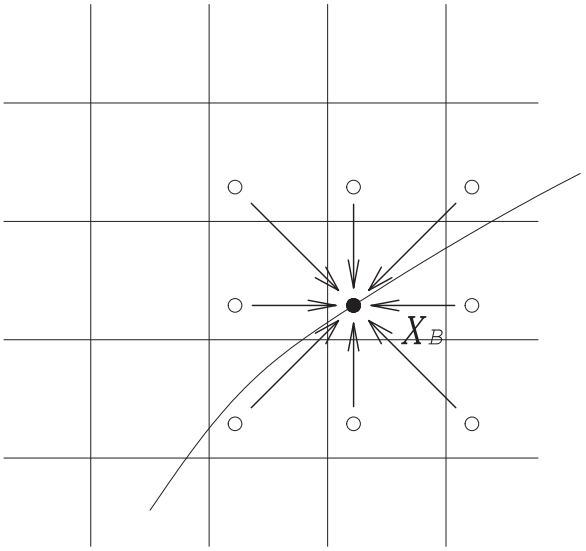

FIG. 1. A schematic illustration of the local grid.

particles with discrete velocity $\mathbf{e}_\alpha$ at the time t_{n-1} within only a curved edge parallelogram could collide with the solid surface element. It is observed that the area (volume) of the curved edge parallelogram approximately is equal to $\Delta V_\alpha = |\Delta t \Delta s_B \mathbf{e}_\alpha \cdot \boldsymbol{n}_B|$. Here s_B,$\boldsymbol{n}_B$ are the length (area) of the arc (area) element and the normal vector at point $\mathbf{X}_B$ respectively. Moreover, the total mass in this parallelogram is $\int_{\Delta V_\alpha} f_\alpha dV$. Of course, the solid particle moves over time, so the area (volume) of fluid particles which hit the arc (area) element is computed using an time averaging approach. $\mathbf{X}(t_n)$ is selected as an average position of the solid particle in the time interval $[t_{n-\frac{1}{2}}, t_{n+\frac{1}{2}}]$.

Now we can understand the basic difference of computing strategy of the mass of fluid particles which hit the solid particle between the present method and the conventional methods. In the original methods, the mass of the fluid particles which collide with the solid particle can be obtained by means of summing the contribution over all relevant discrete velocity directions. However, the mass of the fluid particles which collide with the arc (area) element are computed by an integration method in a control volume. Moreover, we

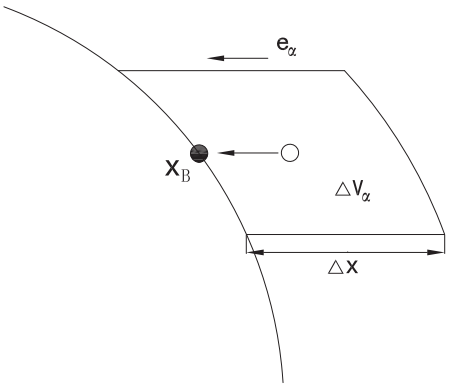

FIG. 2. A schematic illustration of control volume of the fluid particles at time $t_{n-\frac{1}{2}}$.

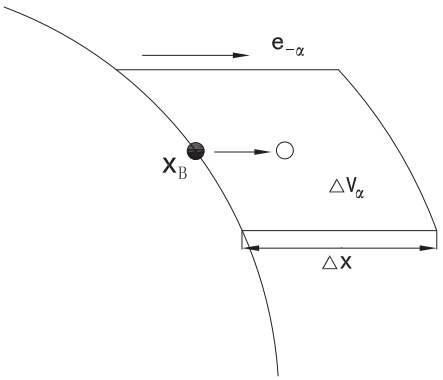

FIG. 3. A schematic illustration of control volume of the fluid particles at time $t_{n+\frac{1}{2}}$.

notice that the force evaluation in conventional methods is discrete velocity dependence. However, in the present method, all discrete velocities are used to compute the fluid-particle interaction force. In Ref. [26] the force oscillation in the previous momentum exchange is explained by the discrete velocity dependence.

Figures 2 and 3 show the state of fluid particles at time $t_{n-\frac{1}{2}}$ and $t_{n+\frac{1}{2}}$. During the collision of fluid particles and solid particles, the momentum of fluid particles will change. The change of the momentum of the fluid particles which collide with the arc (area) element is given by

$$\Delta\mathbf{P}_{-\alpha} = \mathbf{e}_{-\alpha}\int_{V_\alpha} f_{-\alpha}\left(t_{n+\frac{1}{2}}\right)dV - \mathbf{e}_{\alpha}\int_{V_\alpha} f_{\alpha}\left(t_{n-\frac{1}{2}}\right)dV, \quad (13)$$

where $-\alpha$ means the opposite direction of α, namely, $\mathbf{e}_\alpha = -\mathbf{e}_{-\alpha}$. The above integration in a parallelogram can be computed using a numerical technique. The Newton-Cotes quadrature rule or Gauss quadrature formula can be selected. In this paper, a simple formula with single integration point is selected:

$$\int_{\Delta V_\alpha} f_\alpha\, dV \cong f_\alpha\left(\mathbf{X}_B - \mathbf{e}_\alpha\frac{\Delta t}{2}, t_{n-\frac{1}{2}}\right)\Delta V_\alpha, \quad (14)$$

$$\int_{\Delta V_\alpha} f_{-\alpha}\, dV \cong f_{-\alpha}\left(\mathbf{X}_B - \mathbf{e}_\alpha\frac{\Delta t}{2}, t_{n+\frac{1}{2}}\right)\Delta V_\alpha. \quad (15)$$

Using the bounce-back rule, we have

$$f_{-\alpha}\left(\mathbf{X}_B - \mathbf{e}_\alpha\frac{\Delta t}{2}, t_{n+\frac{1}{2}}\right) = f_\alpha\left(\mathbf{X}_B - \mathbf{e}_\alpha\frac{\Delta t}{2}, t_{n-\frac{1}{2}}\right) - 2\omega_{-\alpha}\rho\frac{\mathbf{e}_{-\alpha}\cdot\mathbf{U}(\mathbf{X}_B,t_n)}{c_s^2}. \quad (16)$$

Applying the stream rule, we have

$$f_\alpha\left(\mathbf{X}_B - \mathbf{e}_\alpha\frac{\Delta t}{2}, t_{n-\frac{1}{2}}\right) = f_\alpha(\mathbf{X}_B, t_n). \quad (17)$$

We can get

$$\begin{aligned}\Delta\mathbf{P}_{-\alpha} &\cong \mathbf{e}_{-\alpha}\left[f_{-\alpha}\left(\mathbf{X}_B - \mathbf{e}_\alpha\frac{\Delta t}{2}, t_{n+\frac{1}{2}}\right) + f_\alpha\left(\mathbf{X}_B - \mathbf{e}_\alpha\frac{\Delta t}{2}, t_{n-\frac{1}{2}}\right)\right]V_\alpha \\ &= 2\mathbf{e}_{-\alpha}\left[f_\alpha\left(\mathbf{X}_B - \mathbf{e}_\alpha\frac{\Delta t}{2}, t_{n-\frac{1}{2}}\right) - \omega_{-\alpha}\rho\frac{\mathbf{e}_{-\alpha}\cdot\mathbf{U}(\mathbf{X}_B,t_n)}{c_s^2}\right]V_\alpha \\ &= 2\mathbf{e}_{-\alpha}\left[f_\alpha(\mathbf{X}_B,t_n) - \omega_{-\alpha}\rho\frac{\mathbf{e}_{-\alpha}\cdot\mathbf{U}(\mathbf{X}_B,t_n)}{c_s^2}\right]V_\alpha. \quad (18)\end{aligned}$$

Then the change of momentum of the fluid particles can be obtained using the density distribution function at the time level n. Since point $\mathbf{X}_B$ may be not located at any fixed grid points, an extra interpolation procedure is needed:

$$f_\alpha(\mathbf{X}_B,t_n) = \sum_{\mathbf{x}_i\in S(\mathbf{X}_B,\alpha)} A_{i,\alpha} f_\alpha(\mathbf{x}_i,t_n), \quad (19)$$

where $S(\mathbf{X}_B,\alpha)$ is the interpolation stencil for the point $\mathbf{X}_B$ and the direction α. A_i is the interpolation coefficient for the corresponding interpolation stencil. In this paper, a second-order upwind interpolation is adopted. This interpolation scheme had been applied in the interpolation-supplemented LBM [27]. The closest grid point for $\mathbf{X}_B$ is noted as (x_m, y_n), and we set

$$dx = x_m - X_B, \quad dy = y_n - Y_B. \quad (20)$$

We have

$$S(\mathbf{X}_B,\alpha) = (x_{m+k\cdot md}, y_{n+l\cdot nd}), \quad (21)$$

where

$$md = \mathrm{sgn}(1,dx), \quad nd = \mathrm{sgn}(1,dy), \quad (22)$$

where sgn is the sign function. Once the interpolation stencil is selected, the interpolation coefficients are computed using the Lagrangian formula.

Therefore, the present method slightly increases the computational cost. Moreover, as same as the Ladd's approach, the internal area of the solid is also treated as the computational domain. Compared with the ALD method, the present version is very simple and easy coding. It is worthy noting that Rohde *et al.* developed a volumetric method to deal with moving boundaries, and the computing strategy of mass of fluid particles which hit the particle boundary is similar as the present method [28]. However, the exterior fluid is used only in this method. So a complex local reconstruction procedure is needed. Moreover, the geometric conservation law is difficult to guarantee.

The coupling force which the fluid impose in the particle boundary point $\mathbf{X}_B$ can be obtained by

$$\begin{aligned}\mathbf{F}(\mathbf{X}_B,t_n) &\approx \frac{\int_{t_{n-\frac{1}{2}}}^{t_{n+\frac{1}{2}}}\mathbf{F}(\mathbf{X}_B,t)\,dt}{\Delta t} = -\frac{\sum_\alpha \Delta\mathbf{P}_{-\alpha}(\mathbf{X}_B,t_n)}{\Delta t} \\ &= \mathbf{F}^{\mathrm{in}}(\mathbf{X}_B,t_n) + \mathbf{F}^{\mathrm{out}}(\mathbf{X}_B,t_n), \quad (23)\end{aligned}$$

where $\mathbf{F}^{\mathrm{in}}(\mathbf{X}_B,t_n)$ and $\mathbf{F}^{\mathrm{out}}(\mathbf{X}_B,t_n)$ are the forces which come from the exterior fluid and interior fluid, respectively, and the moment can be computed as follows:

$$\begin{aligned}\mathbf{T}(\mathbf{X}_B,t_n) &= (\mathbf{X}_B - \mathbf{X}_c)\times\mathbf{F}(\mathbf{X}_B,t_n) \\ &= \mathbf{T}^{\mathrm{in}}(\mathbf{X}_B,t_n) + \mathbf{T}^{\mathrm{out}}(\mathbf{X}_B,t_n), \quad (24)\end{aligned}$$

where $\mathbf{X}_c$ is the centroid coordinate of the particle, and $\mathbf{T}^{\text{in}}(\mathbf{X}_B,t_n)$, $\mathbf{T}^{\text{out}}(\mathbf{X}_B,t_n)$ denote the moments which come from the exterior fluid and interior fluid, respectively.

Therefore, the forces and moment which acted on the particle cab be written as

$$\mathbf{F}_{pf}(t_n)=\sum_{\mathbf{X}_B}\mathbf{F}(\mathbf{X}_B,t_n)=\mathbf{F}^{\text{in}}_{pf}(t_n)+\mathbf{F}^{\text{out}}_{pf}(t_n), \quad (25)$$

$$\mathbf{T}_{pf}(t_n)=\sum_{\mathbf{X}_B}\mathbf{T}(\mathbf{X}_B,t_n)=\mathbf{T}^{\text{in}}_{pf}(t_n)+\mathbf{T}^{\text{out}}_{pf}(t_n). \quad (26)$$

For the conventional momentum exchange method, the density distribution function will be updated automatically after the fluid-solid particle collision. However, in the present method, the positions of the fluid particles may be not located at the fixed Eulerian points. Certainly, there exists many local reconstructions to deal with this problem. In the present study, we introduce the force correction method using the smoothed kernel function. This technique is usually used in meshless particle method, immersed boundary method, and front track method. In this paper, the smoothed delta function is used to distribute the physical quantities to the neighboring fixed nodes. As shown in Fig. 4, the following one-dimensional discrete delta function is selected [29]:

$$W_1(x)=\frac{1}{h}\phi(r)=\begin{cases}\frac{3}{8}+\frac{\pi}{32}-\frac{r^2}{4},|r|\leqslant 0.5,\\ \frac{1}{4}+\frac{1-|r|}{8}\sqrt{-2+8|r|-4r^2}\\ -\frac{1}{8}\arcsin(\sqrt{2}(|r|-1)),0.5\leqslant|r|\leqslant 0.5,\\ \frac{17}{16}-\frac{\pi}{64}-\frac{3|r|}{4}+\frac{r^2}{8}\\ +\frac{|r|-2}{16}\sqrt{-14+16|r|-4r^2}\\ +\frac{1}{16}\arcsin\sqrt{2}(|r|-2),1.5\leqslant|r|\leqslant 2.5,\\ 0,2.5\leqslant|r|.\end{cases} \quad (27)$$

where $r=x/h$.

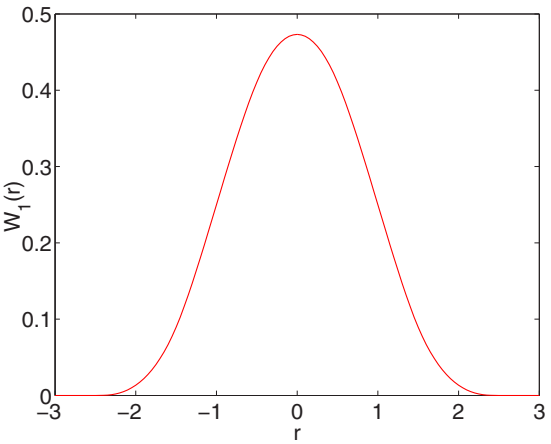

FIG. 4. (Color online) Discrete delta function used in the present study.

The corresponding two- and three-dimensional discrete delta functions can be expressed as

$$W_2(\mathbf{x})=\frac{1}{h^2}\phi\left(\frac{x}{h}\right)\phi\left(\frac{y}{h}\right), \quad (28)$$

$$W_3(\mathbf{x})=\frac{1}{h^3}\phi\left(\frac{x}{h}\right)\phi\left(\frac{y}{h}\right)\phi\left(\frac{z}{h}\right), \quad (29)$$

where $\mathbf{x}=(x,y)$ or (x,y,z).

In fact, once the bounce-back scheme is applied, the coupling force $\mathbf{F}(\mathbf{X}_B)$ at time level n can be utilized to correct the fluid field. Based on Newton's third law, the force acting on the fluid field is expressed as

$$\mathbf{f}(\mathbf{x},t_n)=-\sum_{\mathbf{X}_B}F(\mathbf{X}_B,t_n)w(\mathbf{x}-\mathbf{X}_B). \quad (30)$$

Once we get the above force, the fluid field can be corrected using Eq. (12):

$$\mathbf{u}(\mathbf{x},t_n)=\left[\sum_{\alpha}\mathbf{e}_\alpha f_\alpha(\mathbf{x},t_n)+0.5\mathbf{f}(\mathbf{x},t_n)\Delta t\right]\Big/\rho. \quad (31)$$

C. Particle dynamics

In addition to the force which comes from the fluid, some other forces must be considered. It is critical to compute the particle-particle or wall interaction forces correctly. In this paper, the Lennard-Jones potential is selected, which has been used in Ref. [17] for solving the DKT problem. The particle-particle repulsive force can be expressed as follows:

$$\mathbf{F}^p_{i,j}=\begin{cases}0, & R_{i,j}>R_i+R_j+\zeta,\\ 2.4\varepsilon\sum_{j\neq i}\left[2\left(\frac{R_i+R_j}{R_{i,j}}\right)^{14}-\left(\frac{R_i+R_j}{R_{i,j}}\right)^{8}\right]\frac{\mathbf{R}_i-\mathbf{R}_j}{(R_i+R_j)^2}, & \\ R_{i,j}\leqslant R_i+R_j+\zeta,\end{cases} \quad (32)$$

where R_i is the radius of the ith particle. $R_{i,j}=|\mathbf{R}_i-\mathbf{R}_j|$ is the distance of the centroid between ith particle and jth particle. $\varepsilon=\frac{2R_iR_j}{R_i+R_j}$ is the depth of the potential well. ζ is the critical distance, which is set as $\zeta=\Delta x$ in this paper, and the particle-wall interaction can be obtained by

$$\mathbf{F}^w_{i,j}=\begin{cases}0, & R_{i,w}>2R_i+\zeta,\\ 2.4\varepsilon\sum\left[2\left(\frac{R_i}{R_{i,w}}\right)^{14}-\left(\frac{R_i}{R_{i,w}}\right)^{8}\right]\frac{\mathbf{R}_i-\mathbf{R}_w}{(R_i)^2}, & \\ R_{i,w}\leqslant 2R_i+\zeta,\end{cases} \quad (33)$$

where $R_{i,w}$ is the distance between ith particle and the wall. Obviously, different from the other particle or wall-particle interactions models, the above model does not include any artificial parameters.

The governing equations of particle motion are given by

$$M_p\frac{d\mathbf{U}_p}{dt}=\mathbf{F}_p, \quad (34)$$

$$I_p\frac{d\mathbf{\Omega}_p}{dt}=\mathbf{T}_p, \quad (35)$$

$$\frac{d\mathbf{X}_c}{dt}=\mathbf{U}_p, \quad (36)$$

$$\frac{d\theta_p}{dt}=\mathbf{\Omega}_p, \quad (37)$$

where M_p and I_p are the mass and moment of inertia of the particle, respectively. $\mathbf{U}_p, \mathbf{\Omega}_p$ are the translational velocity and rotational velocity of the particle. θ_p is the angle of the particle. The total force $\mathbf{F}_p$ and moment $\mathbf{T}_p$ acting on the particle are written as

$$\mathbf{F}_p = \mathbf{F}_{pf}^{\text{out}} + \mathbf{F}_{pp} + \mathbf{F}_{pw}, \tag{38}$$

$$\mathbf{T}_p = \mathbf{T}_{pf}^{\text{out}}. \tag{39}$$

Clearly, we notice that $\mathbf{F}_{pf}$ is more easily calculated than $\mathbf{F}_{pf}^{\text{out}}$. So we note that

$$\mathbf{F}_p^{\text{tol}} = \mathbf{F}_{pf} + \mathbf{F}_{pp} + \mathbf{F}_{pw}, \tag{40}$$

$$\mathbf{T}_p^{\text{tol}} = \mathbf{T}_{pf}; \tag{41}$$

we have

$$\mathbf{F}_p = \mathbf{F}_p^{\text{tol}} - \mathbf{F}_{pf}^{\text{in}}, \tag{42}$$

$$\mathbf{T}_p = \mathbf{T}_p^{\text{tol}} - \mathbf{T}_{pf}^{\text{in}}. \tag{43}$$

Moreover, the following equations hold:

$$M_f \frac{d\mathbf{U}_p}{dt} = \mathbf{F}_{pf}^{\text{in}}, \tag{44}$$

$$I_f \frac{d\mathbf{\Omega}_p}{dt} = \mathbf{T}_{pf}^{\text{in}}. \tag{45}$$

Therefore, we have

$$\left(\frac{\rho_p}{\rho_f} - 1\right)\frac{d\mathbf{U}_p}{dt} = \frac{\mathbf{F}_p^{\text{tol}}}{M_f}, \tag{46}$$

$$\left(\frac{\rho_p}{\rho_f} - 1\right)\frac{d\mathbf{\Omega}_p}{dt} = \frac{\mathbf{T}_p^{\text{tol}}}{I_f}, \tag{47}$$

where ρ_p and ρ_f mean the density of the particle and fluid, respectively. In Ladd's method, the leapfrog scheme is used to solve Eqs. (46) and (47). The following condition must be satisfied when the leapfrog scheme is applied:

$$\frac{\rho_p}{\rho_f} > 1 + \frac{10\Delta x}{R_p}. \tag{48}$$

To get a more stable scheme, Aidun *et al.* proposed an improved version [4]. In this method, only exterior fluid nodes are used. However, the complex local construction at the fluid or solid nodes must be considered. In addition, Lowe *et al.* developed an implicit method to overcome this drawback. Obviously, the implicit scheme does need more computational overhead.

In this paper, inspired by Feng and Michaelides [21], we propose a generalized explicit three-time-level difference scheme:

$$\lambda\frac{d\mathbf{U}(t_{n+1})}{dt} \cong \frac{a\mathbf{U}(t_{n+1}) - b\mathbf{U}(t_n) - c\mathbf{U}(t_{n-1})}{\Delta t}, \tag{49}$$

$$b = 2a - \lambda, \tag{50}$$

$$c = \lambda - a, \tag{51}$$

where $\lambda = \rho_p/\rho_f - 1$. a is a positive number. We introduce a critical value ς of λ. When λ is larger than ς, a is set as $a = 3\lambda$. Conversely, a relatively large positive number can be selected to assign to a when λ is less than ς. In this paper, ς is set as 0.2 in all numerical examples.

Equations (34)–(37) are solved as follows:

$$\mathbf{U}_p(t_{n+1}) = \left[b\mathbf{U}_p(t_n) + c\mathbf{U}_p(t_{n-1}) + \frac{\Delta t\mathbf{F}_p^{\text{tol}}(t_n)}{M_p}\right]\Big/ a, \tag{52}$$

$$\mathbf{\Omega}_p(t_{n+1}) = \left[b\mathbf{\Omega}_p(t_n) + c\mathbf{\Omega}_p(t_{n-1}) + \frac{\Delta t\mathbf{T}_p^{\text{tol}}(t_n)}{I_p}\right]\Big/ a, \tag{53}$$

$$\mathbf{X}_c(t_{n+1}) = \mathbf{X}_c(t_n) + \frac{1}{2}[\mathbf{U}_p(t_{n+1}) + \mathbf{U}_p(t_n)]\Delta t, \tag{54}$$

$$\theta_p(t_{n+1}) = \theta_p(t_n) + \frac{1}{2}[\mathbf{\Omega}_p(t_{n+1}) + \mathbf{\Omega}_p(t_n)]\Delta t. \tag{55}$$

We can increase the value of a to ensure the stability of the above computational procedure:

Once get the translational velocity $\mathbf{U}_p^{n+1}$ and rotational velocity $\mathbf{\Omega}_p^{n+1}$ at the time level $n+1$, the velocity of boundary point are computed as follows:

$$\mathbf{U}(\mathbf{X}_B) = \mathbf{U}_p + \mathbf{\Omega}_p \times (\mathbf{X}_B - \mathbf{X}_c), \tag{56}$$

III. RESULTS AND DISCUSSION

To test the performance of the present momentum exchange method, some two- and three-dimensional problems are simulated in the following.

A. Circular-particle sedimentation

Single-circular-particle sedimentation is a classical problem. Many scholars have investigated this problem using different methods. First, the numerical simulation for particle settling in an infinite channel is considered. The ratio of channel width and particle diameter is set as $W* = W/D = 4$. When the ratio of particle density to fluid density ρ_p/ρ_f is very close to 1, compared with the effect of the fluid viscosity, the effect of inertia is weak. The terminal velocity of the particle can be computed using the following approximately analytical solution:

$$u_t = \frac{D^2}{16K\nu}\left(\frac{\rho_p}{\rho_f} - 1\right)g, \tag{57}$$

where g is the gravitational acceleration, and the coefficient K is given by Happel and Brenner [30].

In the present study, $K = 1.747\,86$ can be obtained when $W^* = 4$. The cases with $\rho_p/\rho_f = 1.000\,01, 0.999\,99$ are investigated to test the modified momentum exchange method and particle motion scheme. The viscosity and gravitational acceleration are fixed to be $\nu = 0.08$ cm/s^2, $g = 980$ cm/s^2. In fact, the computational procedures are stable for different a in the Eq. (49). As shown in Table I, the present numerical solutions with $a = 0.3, 0.5$ show good agreement with the

TABLE I. Comparison of the terminal velocity between the numerical solutions and analytical solutions.

ρ_p/ρ_f	1.000 01	0.999 99
Analytical solutions	-4.4380×10^{-3}	4.4380×10^{-3}
$a = 0.5$	-4.4338×10^{-3}	4.4340×10^{-3}
$a = 0.8$	-4.4319×10^{-3}	4.4317×10^{-3}

analytical solutions. We notice that the ratio of particle to fluid densities in this case is very close to 1 or less than 1. The numerical results indicate that the present explicit scheme can remove the restriction of ratio of particle to fluid densities in the shell model and the present method is robust. In the following simulations, $a = 0.8$ is selected.

Second, a circular particle falls in a bounded cavity is considered. A rectangular computational domain with a size of 2 cm $\times$ 6 cm is used. A particle with diameter of 0.25 cm is located at (1 cm,4 cm) at the initial time. Compared with the above cases with density ratio is close to 1, two different heavy particles with $\rho_p = 1.25$ g/cm^2, 1.5 g/cm^2 are tested. The density of fluid is set as $\rho_f = 1.0$ g/cm^2. The viscosity μ is either 0.1 cm^2/s or 0.01 cm^2/s.

A 200×600 grid is used to carry out our simulation. Figure 5 plots the time history for the y coordinate of the center of the particle for $\rho_p = 1.25$ g/cm^2 and $\nu = 0.1$ cm^2/s, and Fig. 6 presents the change of y coordinate of the translation velocity of the particle over time. Obviously, the particle quickly reaches the terminal velocity in a short time. When the particle hits the bottom, the velocity of the particle fall to zero quickly. It can be observed that a good agreement is achieved between the present results and the results of Wan *et al.* and Glowinski *et al.* [31,32]. Moreover, another case with $\rho_p = 1.5$ g/cm^2, $\nu = 0.01$ cm^2/s is also simulated. As shown in Figs. 7 and 8, both position and velocity of the particle are in line with the results of Glowinski *et al.* [32].

Third, the sedimentation of a circular cylinder which is located away from the center line in a vertical channel is simulated. Compared with the above single-particle-sedimentation

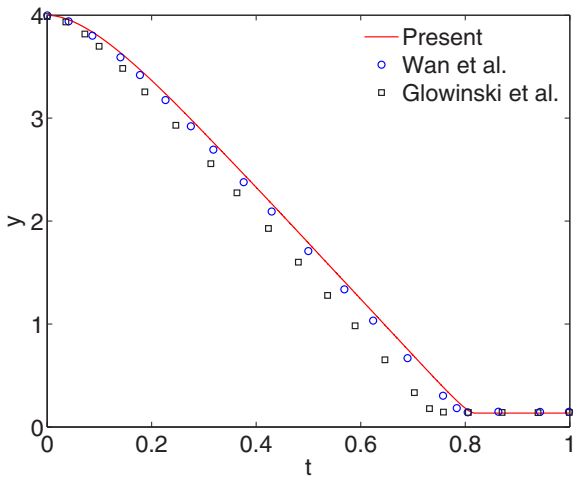

FIG. 5. (Color online) Histories for the y coordinate of the center of the particle for $\rho_p = 1.25$ g/cm^2 and $\nu = 0.1$ cm^2/s.

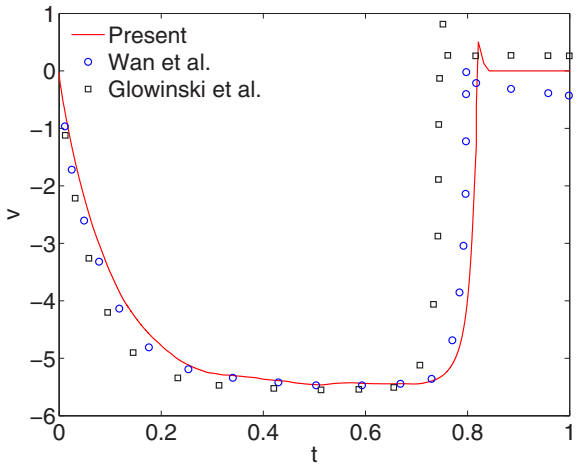

FIG. 6. (Color online) Histories for the y coordinate of the translation velocity of the particle for $\rho_p = 1.25$ g/cm^2 and $\nu = 0.1$ cm^2/s.

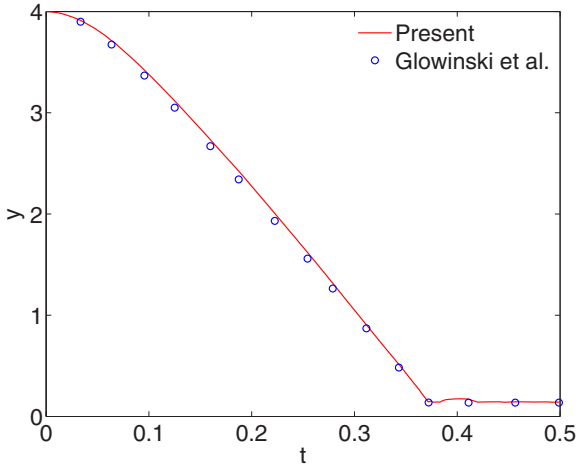

FIG. 7. (Color online) Histories for the y coordinate of the center of the particle for $\rho_p = 1.5$ g/cm^2 and $\nu = 0.01$ cm^2/s.

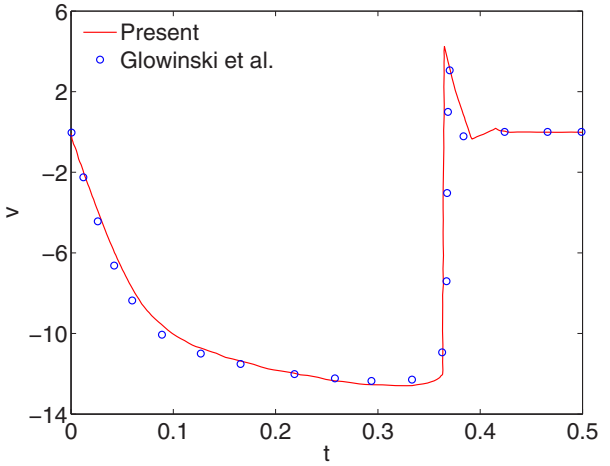

FIG. 8. (Color online) Histories for the y coordinate of the translation velocity of the particle for $\rho_p = 1.5$ g/cm^2 and $\nu = 0.01$ cm^2/s.

problems, the moment equation (47) plays an important role during the motion of particle. Wen *et al.* and Li *et al.* studied this problem [5,33]. In this paper, the numerical results by Hu *et al.* which are obtained by the arbitrary Lagrangian-Eulerian method (ALE) are adopted as the benchmark solutions [34].

The channel of 2 cm width and 8 cm height is used as the computational domain. The cylinder with radius $r_p = 0.1$ cm is initially located at 0.076 cm,1 cm away from the left wall and top wall, respectively. The fluid density and kinematic viscosity are set to be 1 g/cm^3 and 0.01 cm^2/s, respectively. Four different cases with different solid-fluid ratios 1.0015,1.003,1.01,1.03 are studied. The solid-fluid ratios in these cases are very close to 1, so the generalized explicit time marching scheme with $a = 0.8$ (49) is used.

The computational domain is divided into 200×800 grid cells. As shown in Fig. 9, the particle trajectories for different cases are presented. Clearly the present results show good agreement with the FEM data. However, the curved boundary-based method (CBM) [10] deviates significantly from the present method and ALE method. Figure 10 plots the particle velocities in a horizontal direction for different cases. The correct particle dynamics can be obtained using the present method. It indicates that the present force evaluation method has very high

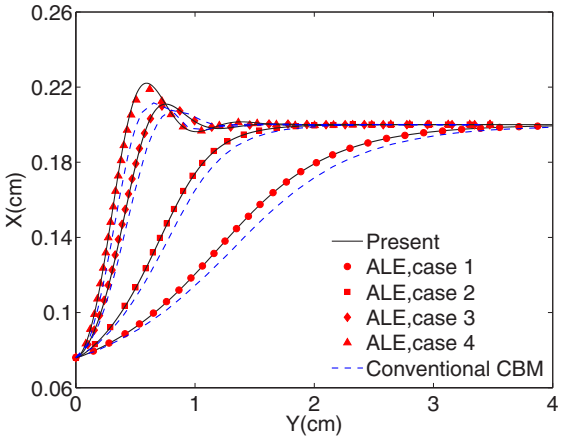

FIG. 9. (Color online) Comparison of the particle trajectories for different cases.

$$K = \frac{1}{\ln W^* - 0.9157 + 1.7244(W^*)^{-2} - 1.7302(W^*)^{-4} + 2.4056(W*)^{-6} - 4.5913(W^*)^{-8}}. \quad (58)$$

accuracy and reliability.

B. Circular particle motion in the shear flows

To test the Galilean invariance of the present method, the problem of circular particle motion in the shear flows is simulated. Some works have discussed this issue [6,8,26,35]. The present numerical example is the same as that in the Ref. [6]. As shown in Fig. 11, a rectangular channel with the size of 500×100 is chosen as the computational domain. The circular disk is located in the middle of the channel. The radius of the circular disk is set as $r_p = 0.1$, and the density ratio of the particle and fluid is fixed at $\rho_p/\rho_f = 3.0$. The velocities on the top and bottom walls are $U_x + \frac{\dot{\gamma}H}{2}$ and $U_x - \frac{\dot{\gamma}H}{2}$, respectively. Here $\dot{\gamma}$ is the shear rate. The fluid velocity is changing in a linear fashion along the y direction. If the numerical method does not break the Galilean invariance, the y component of the particle-fluid interaction force should be able to be negligible.

As same as the Ref. [6], the value of translational velocity U_x and shear rate $\dot{\gamma}$ change separately. Moreover, the force acting on the particle is computed using a time-average method. As shown in Fig. 11(a), the translational velocity U_x is fixed at 0.05. As shown in Fig. 12(a), for the conventional bounce-back method (BBM) [1–3] and curved boundary-based method (CBM)[10], the y direction force F_y is linearly related to the shear rate. Compared with conventional methods, F_y is kept almost unchanged as the shear rate $\dot{\gamma}$ increase in the present method. It indicates that the Galilean invariance is satisfied in the modified momentum exchange method. Figure 12(b) depicts the correlation between the F_y and the translational velocity in three methods. The same conclusion can be obtained in this case.

C. Elliptical-particle sedimentation

Different from the circular particle, the elliptical particle is anisotropic. Therefore, elliptical particle is more sensitive to the numerical errors. When an elliptical particle falls in a narrow channel, the flow field is more complex. As same as the Ref. [6], the numerical results of Xia *et al.* which are obtained by the finite element method are used for benchmark comparison [36]. In this paper, a rectangular computational domain with a size of $L \times 30L = 0.4$ cm $\times$ 12 cm is adopted. The density and kinematic viscosity of the fluid are set as $\rho_f = 1.0$ g/cm^2, $\nu = 1.0 \times 10^{-2}$ cm^2/s. The gravitational acceleration is $g = 980$ cm/s^2. The sizes of major and minor axes of the elliptical particle are $a = 0.05$ cm, $b = 0.025$ cm. As in the previous literature [36], the density ratio of the solid particle and fluid is set as $\rho_p/\rho_f = 1.1$.

The grids with $L = 104$ and 208 lattice units are used for this case. In the initial time, the center of elliptical particle is located at 2 cm from the top wall, and its coordinate is set as (0.2 cm,0 cm). The initial angle of deviation is $\pi/4$. The nonslip boundary condition is imposed on the four outer walls of the computational domain.

In Figs. 13 and 14 the particle trajectories and orientations are compared. In Ref. [6], Chen *et al.* evaluates some typical momentum exchange methods. It indicates the corrected momentum exchange method proposed by them and Caiazzo *et al.* are superior over others. So in addition to the data of Xia *et al.* [36], the computational results which are obtained using

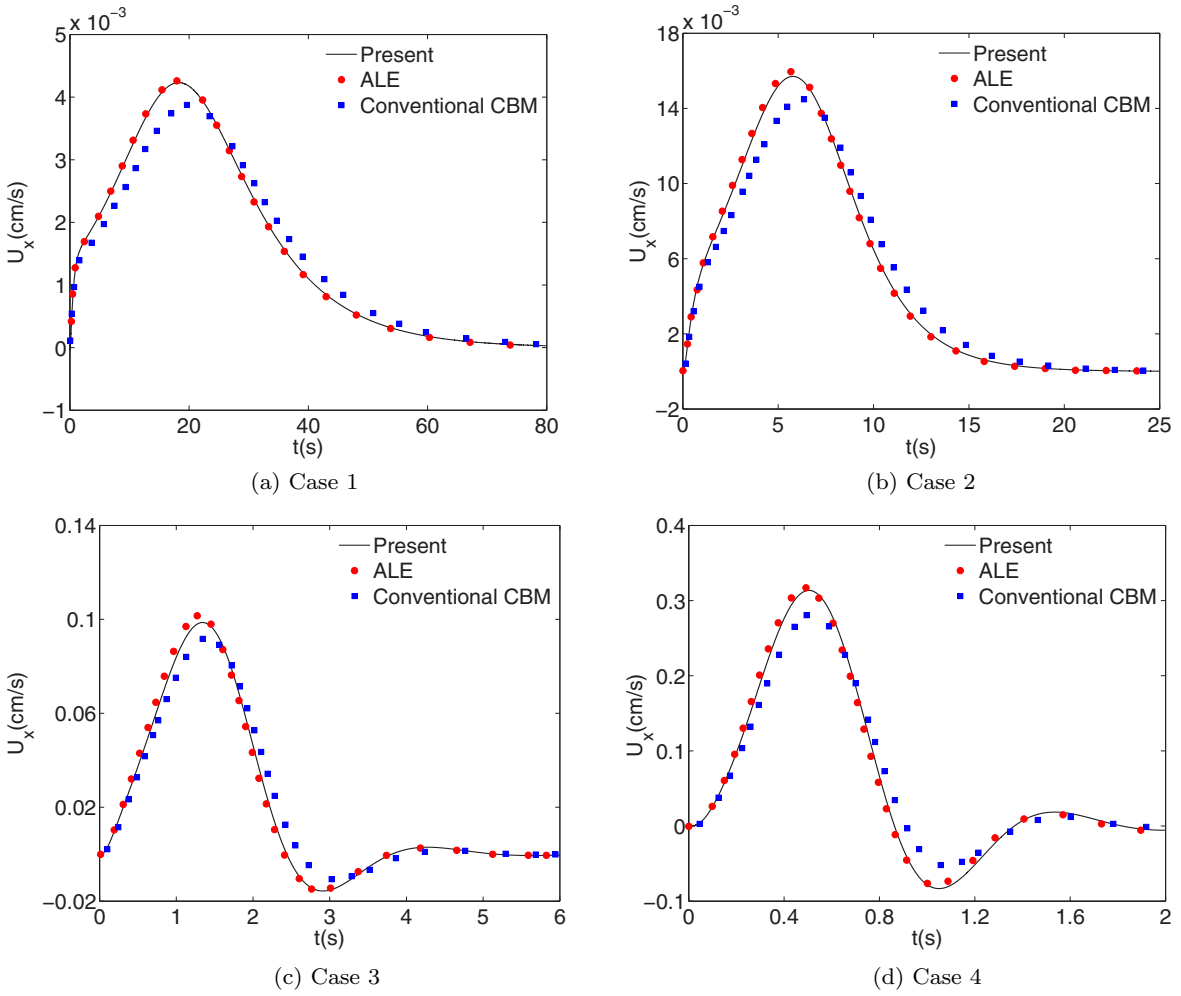

FIG. 10. (Color online) Comparison of the particle velocities in the x direction for different cases.

the corrected momentum exchange methods [6,26] are also adopted. Obviously, the present results which are computed in the coarse grid ($L = 104$ lattice units) slightly deviate from the other results. However, when the grids become finer ($L = 208$ lattice units), the present results show good agreements with the other numerical results. In Fig. 15 the fluid force acting on the particle during the quasi steady state obtained by the above momentum exchange methods is presented. Although some corrected terms are added in the momentum exchange method of Chen *et al.* and Caiazzo *et al.*, the force still fluctuates to some degree. However, the force obtained by the present method is very smooth. The smooth mechanism of the present method roots from (30).

In addition, we also investigate the effect of different density ratios. Four different particle densities, $\rho_p = 1.01\ \mathrm{g/cm^2}$, $1.1\ \mathrm{g/cm^2}$, $1.3\ \mathrm{g/cm^2}$, $1.5\ \mathrm{g/cm^2}$, are selected. In the cases with low-density ratios, $\rho_p = 1.01\ \mathrm{g/cm^2}, 1.1\ \mathrm{g/cm^2}$, a is set as 0.8 in Eq. (49). In Fig. 16 we compare the vertical velocities of sedimentation for different density ratios with the results by Xia *et al.* [36]. It can be observed that

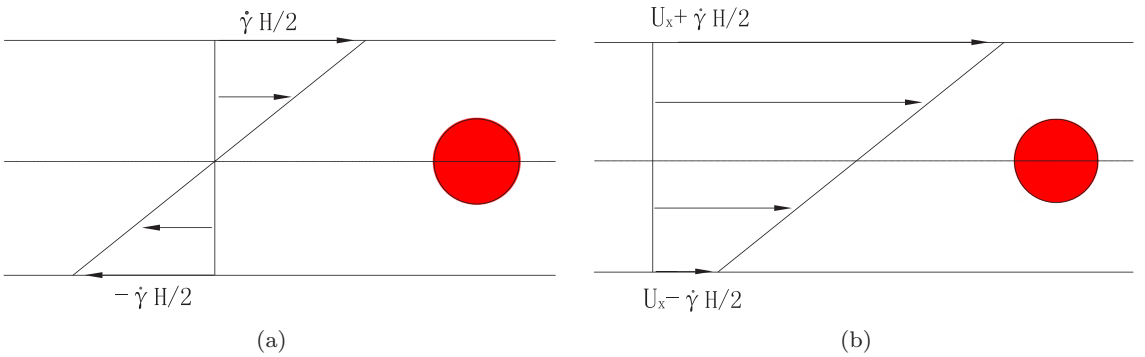

FIG. 11. (Color online) The geometry configuration of the problem used to check the Galilean invariance of the present method.

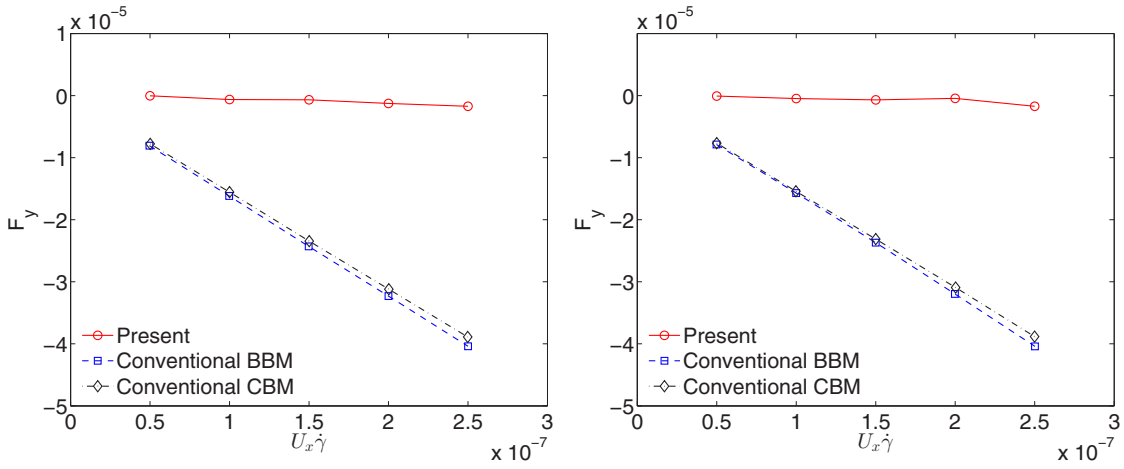

(a) $U_x = 0.01$ (b) $\dot{\gamma} = 2.5 \times 10^{-5}$

FIG. 12. (Color online) The shear flow test used to check the Galilean invariance.

the terminal velocities with low-density ratios keep stable. However, in the case of high-density ratios, the terminal velocities are periodically oscillatory. Moreover, the present results are in good agreement with the numerical results of Xia *et al.* [36].

D. A sphere settling in a cavity

To test the capacity of the present momentum exchange method to simulate three-dimensional flows, the simulation on a single-sphere settling under gravity are presented. The numerical results will be compared with the experimental results which are provided by Cate *et al.* [37]. The experimental data are measured by using the PIV system. As shown in Fig. 17, a rectangular cavity with sizes 10 cm × 10 cm × 16 cm is chosen as the computational domain. The radius of the sphere is $r_p = 0.75$ cm, and the density of this sphere is fixed at $\rho_p = 1.12\ \mathrm{g/cm^3}$. The initial position of the center of sphere is set to (5 cm,5 cm,12.75 cm).

In this simulation, four cases with different fluid densities and dynamic viscosities are considered. The fluid densities $\rho_f(\mathrm{g/cm^2})$ and dynamic viscosities $\mu_f[/(\mathrm{cm}\cdot\mathrm{s})]$ are set to be

Case 1: $(\rho_f,\mu_f) = (0.97,3.73)$,
Case 2: $(\rho_f,\mu_f) = (0.965,2.12)$,
Case 3: $(\rho_f,\mu_f) = (0.962,1.13)$,
Case 4: $(\rho_f,\mu_f) = (0.96,0.58)$.

Before our simulation, the surface of the sphere must be divided to a set of control domain. In this paper, the points distribution method proposed by Saff and Kuijlaars [38] is applied. Using the spherical coordinates (θ,ϕ,r_p), we have

$$\theta_k = \arccos(h_k), \quad h_k = -1 + \frac{2(k-1)}{N-1}, \quad 1 \leqslant k \leqslant N, \tag{59}$$

$$\phi_1 = \phi_N = 0, \quad \phi_k = \phi_{k-1} + \frac{3.6}{\sqrt{N\left(1-h_k^2\right)}}, \quad 1 < k < N, \tag{60}$$

where N is the number of the points.

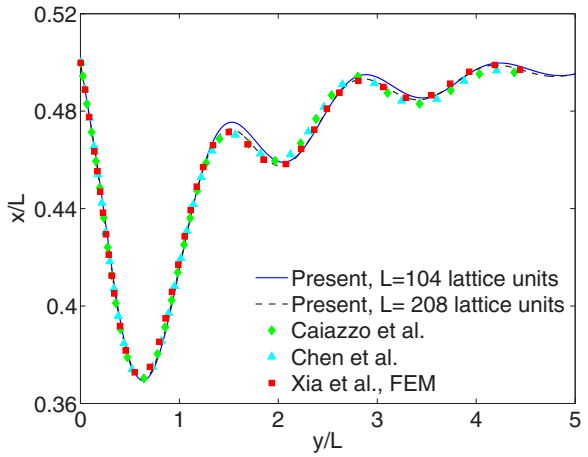

FIG. 13. (Color online) Comparison of trajectories of the center of the elliptical particle.

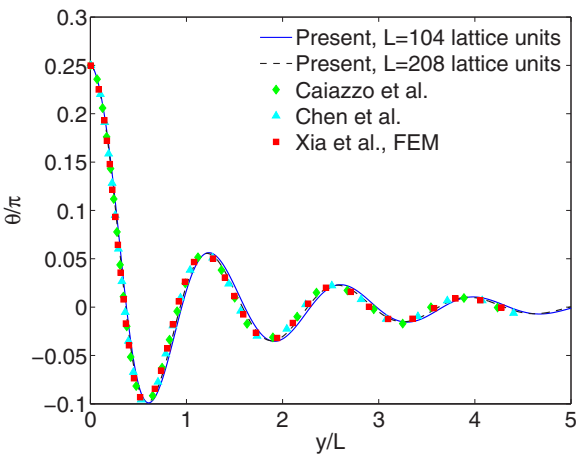

FIG. 14. (Color online) Comparison of orientation of the elliptical particle.

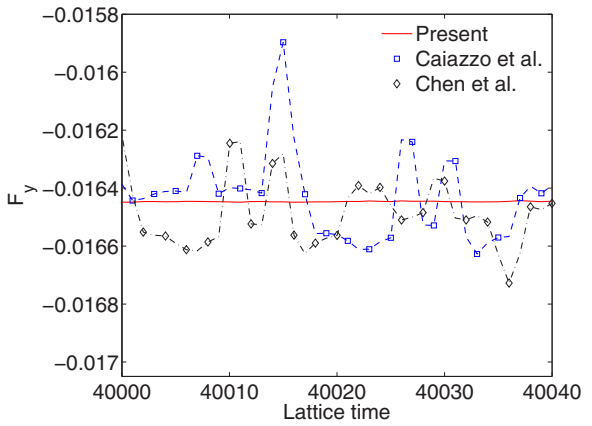

FIG. 15. (Color online) Comparison of the y component force, which acts on the particle during the terminal settling state.

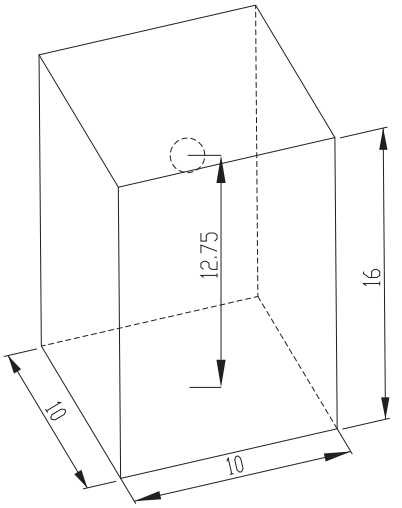

FIG. 17. Schematic diagram for a sphere setting in a cavity.

In the present method, the volume of the curved edge parallelogram depends on the lattice models. So the numerical results which are computed using the D3Q15 and D3Q19 models are compared. As shown in Fig. 18, for case 3, the particle settling velocities which are obtained by the same grid ($120 \times 120 \times 192$) while using different lattice models are compared. Obviously, no significant differences are revealed between them. It indicates the present method does not depend on the specific model. Considering the computational efficiency, the D3Q15 model is used in the following section.

In Fig. 19 the effect of grid refinement for the present method is tested. As the mesh becomes finer, the final sedimentation velocity of the particle becomes larger. As a compromise between accuracy and efficiency, the $120 \times 120 \times 192$ grid is adopted in this study. The numerical results of using this grid can be acceptable.

As shown in Fig. 20, the z direction velocities of the particle as the function of time are presented. The present simulation results agree very well with the experimental data. It can be observed that the present falling velocities are slightly larger than the experimental values for all cases. We also notice that the largest differences between the experiment and simulation results are found for case 4. A similar phenomenon is also observed in Ref. [39–41] (IBM). The reason may be that the smoothed technique is adopted in IBM and the present momentum exchange method. It could result in large numerical

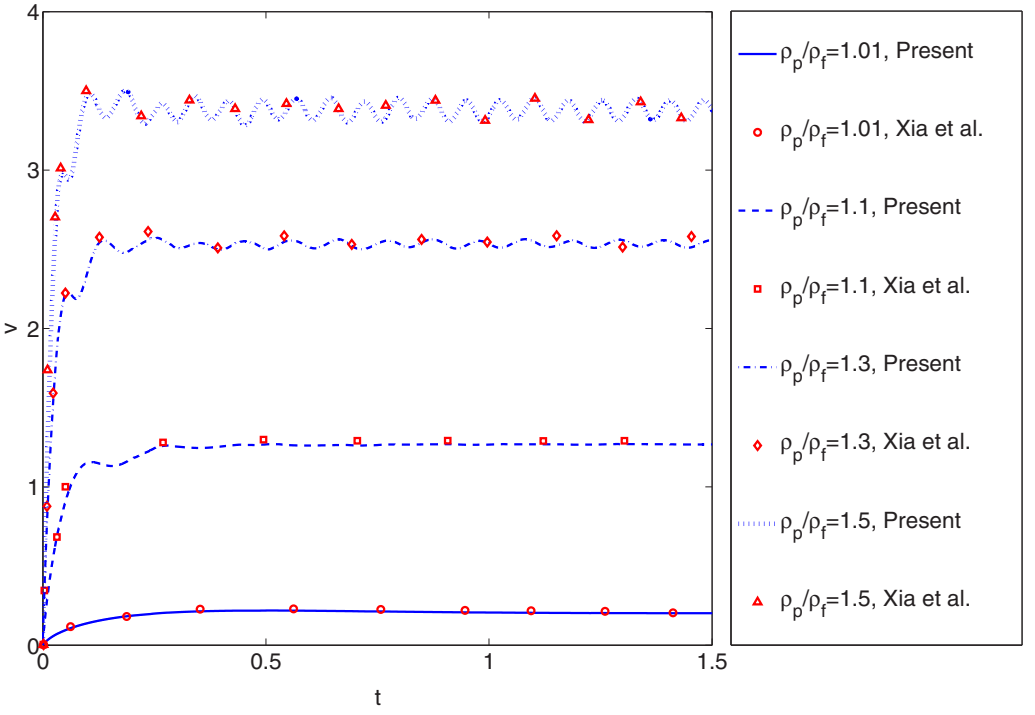

FIG. 16. (Color online) Comparison of terminal velocity of the elliptical particle.

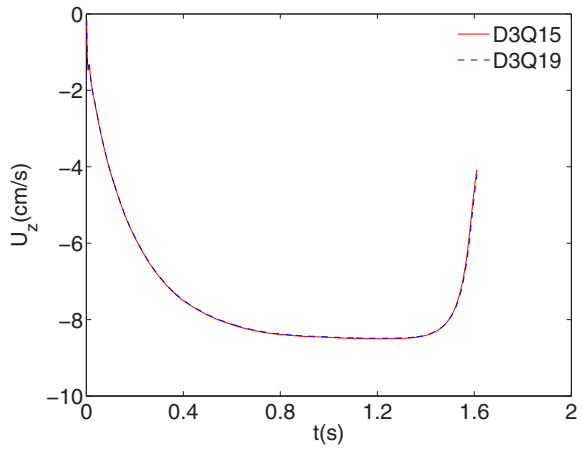

FIG. 18. (Color online) Comparison of particle settling velocity for case 3 while using the D3Q15 and D3Q19 models.

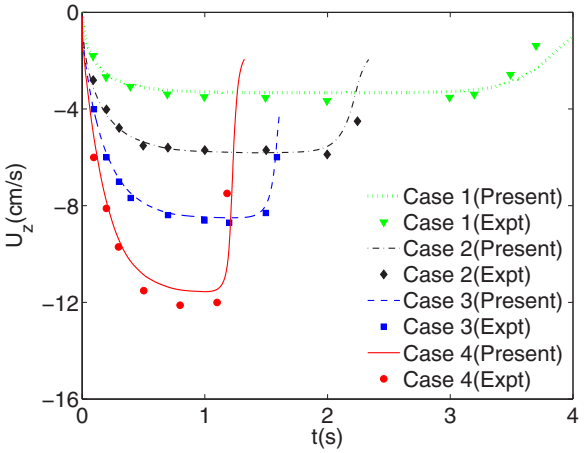

FIG. 20. (Color online) Comparison of particle settling velocity with the experimental data for different cases.

dissipation and the numerical viscosity playing an important role in the simulation.

E. The DKT motion

In the fluid-particle coupling system, except for the direct interaction such as particle-particle collision, the fluid can be a medium to deliver the interaction of the particle. In this case, the interaction is indirect. A classical problem is the two-particle sedimentation. When two particles become close, the drafting, kissing, and tumbling phenomenon (DKT) will appear. In fact, when the leading particle moves down, a low-pressure area will generate above the leading particle. The fluid resistance acting on the trailing particle is smaller than the leading one. So it moves more faster. The two particles will be close to each other. After some period, the two particles will contact each other. Due to the instability of the contact position, the particles will tumble. In this case, the leading particle will move with a large lateral velocity, and trailing particle overtakes the leading one. The DKT motion was studied by Fortes *et al.* using the experimental method [42]. In this paper, we compare our results with numerical results by Feng *et al.* [43].

In this simulation, the density of the fluid and particle is set as $\rho_f = 1.0\ \mathrm{g/cm^2}$, $\rho_p = 1.01\ \mathrm{g/cm^2}$. The viscosity of the fluid is $\nu = 0.01\ \mathrm{cm^2/s}$, and the gravitational acceleration is $g = 980\ \mathrm{cm/s^2}$. Two particles are inside a rectangle channel with a size of 2 cm × 8 cm. The initial positions of the particles are set as (0.999 cm, 7.2 cm) and (1.0 cm, 6.8 cm), respectively. The simulation starts with zero velocity condition. The nonslip wall boundary condition is used. The computational domain is divided into 200 × 800 lattice units.

As shown in Figs. 21 and 22, the transverse and longitudinal coordinates of the centers of the two particles are plotted. It can be observed that the present curves and the results of Feng *et al.* are almost coincident before two particles make contact. Analogously, in Figs. 23 and 24, the transverse and longitudinal velocities of the particles are very close until the two particle collide. The motion of the two particles shows significant differences between the present results and the results of Feng *et al.* [43]. One reason which leads to the differences is that different collision models are used. As

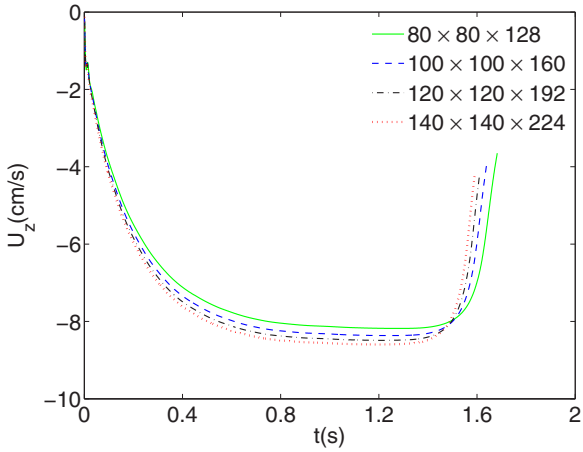

FIG. 19. (Color online) Comparison of particle settling velocity for case 3 when different grid sizes were used.

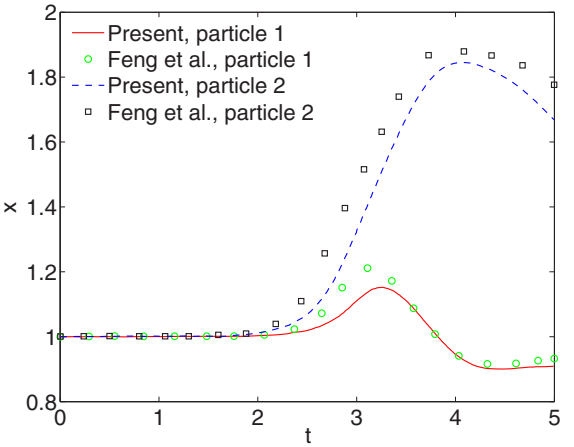

FIG. 21. (Color online) X component of coordinates of the centers of the two particles.

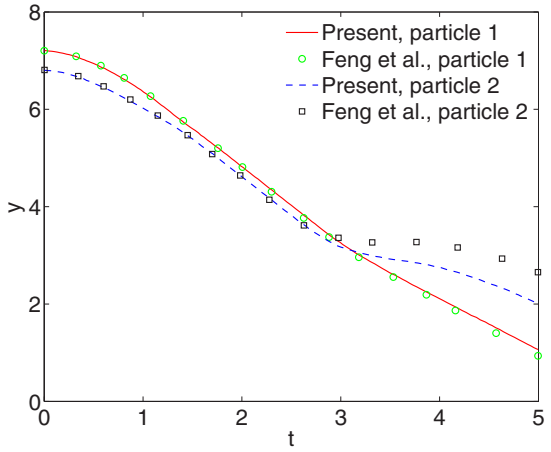

FIG. 22. (Color online) Y component of coordinates of the centers of the two particles.

Fortes *et al.* pointed out, another reason is the instability of the particles' contact position [42].

To describe the details of the DKT motion, we investigate the change of the distance dr of the centers between two particles. dr is defined as

$$dr = \sqrt{(xc_1 - xc_2)^2 + (yc_1 - yc_2)^2}, \tag{61}$$

where xc_1, xc_2, yc_1, yc_2 are the x component and y component of coordinates of the centers of the two particles, respectively.

As shown in Fig. 25, the evolution of the distance of centers between two particles falls into three stages according to its motion characteristics:

(1) Falling independently

At $0 < t < 0.5$ s, the distance of the centers of two particles is almost unchanged because it will take time to spread the disturbance of the fluid. The settlement of two particles is uncorrelated at this stage.

(2) Drafting

At $0.5s \leqslant t \leqslant 1.32$ s, the leading particle moves more slowly than the trailing particle. Hence the distance decreases as time goes on.

(3) Kissing

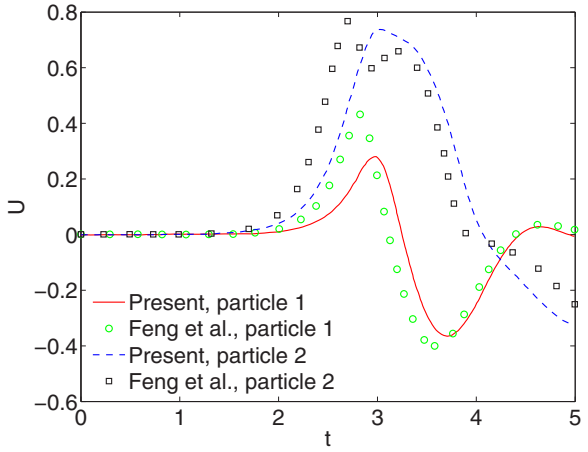

FIG. 23. (Color online) X component of velocities of the two particles.

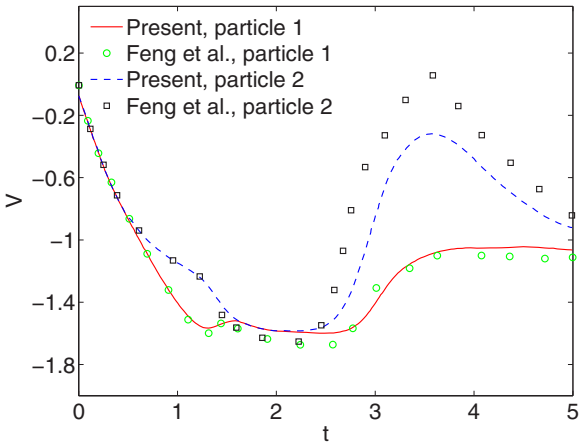

FIG. 24. (Color online) Y component of velocities of the two particles.

At $t \approx 1.32$ s, the two particles collide at this moment. The distance has become minimized.

(4) Tumbling

At $1.32s \leqslant t \leqslant 2.5$ s, the particles begin to tumble. However, the particles fit closely together. So the distance remains approximately constant during this period.

(5) Separating

At $t > 2.5$ s, two particles begin to separate and the distance increases.

IV. CONCLUSION

In the present work, a simple and efficient momentum exchange method based on the lattice Boltzmann method is developed to simulate the fluid-particle interactions. The real curved boundary can be captured using the present momentum exchange method. Therefore, the shape of the particle can be ensured during the simulations. The change of momentum on an arc (area) element is computed using a strategy which considers some control volumes in which the fluid particles would hit the arc (area) element during a certain period. The fluid field is corrected by the force, which distributed from the boundary marker points using an assigning function. For the density

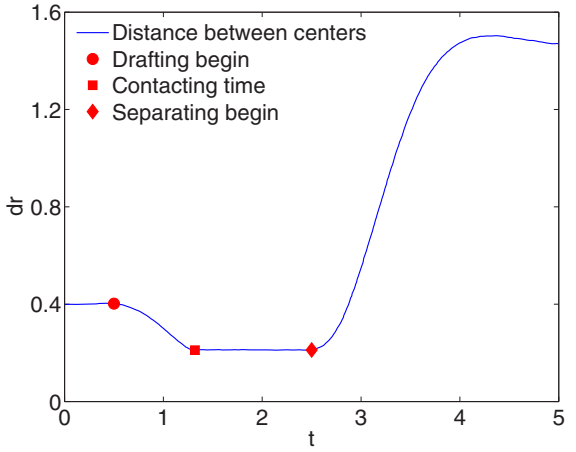

FIG. 25. (Color online) The time evolution of distance of the centers between two particles.

ratio between particle and fluid close to 1 or less than 1, we propose a three-time-level scheme to resolve the motion of the particle.

Numerical simulations of several two- and three-dimensional sedimentation problems have been carried out to test our scheme. The present results show good agreements with the previous studies. It can be observed that the present method is capable of simulating the complex coupled fluid-particle interaction system.

ACKNOWLEDGMENTS

This research was supported by the National Natural Science Foundation of China (Grant No. 51375039), Beijing Natural Science Foundation (Grant No. 4142046), Program for Changjiang Scholars and Innovative Research Team in University (Grant No. IRT13046, IRT1179) and Specialized research Fund for the Doctoral Program of Higher Education (20124301110003). Y.H. also thanks Hao Zhang for his help in improving our paper.

[1] A. J. C. Ladd, J. Fluid Mech. **271**, 285 (1994).
[2] A. J. C. Ladd, J. Fluid Mech. **271**, 311 (1994).
[3] A. J. C. Ladd and R. Verberg, J. Stat. Phys. **104**, 1191 (2001).
[4] C. K. Aidun and Y. N. Li, J. Stat. Phys. **81**, 49 (1995).
[5] B. Wen, H. Li, C. Zhang, and H. Fang, Phys. Rev. E **85**, 016704 (2012).
[6] Y. Chen, Q. Cai, Z. Xia, M. Wang, and S. Chen, Phys. Rev. E **88**, 013303 (2013).
[7] D. W. Qi, J. Fluid Mech. **385**, 41 (1999).
[8] E. Lorenz, A. Caiazzo, and A. G. Hoekstra, Phys. Rev. E **79**, 036705 (2009).
[9] O. Filippova and D. Hänel, Comput. Fluids **26**, 697 (1997).
[10] R. Mei, L. Luo, and W. Shyy, J. Comput. Phys. **155**, 307 (1999).
[11] M. Bouzidi, M. Firdaouss, and P. Lallemand, Phys. Fluids **13**, 3452 (2001).
[12] Z. L. Guo, C. G. Zheng, and B. C. Shi, Phys. Fluids **14**, 2007 (2002).
[13] P. Lallemand and L. Luo, J. Comput. Phys. **184**, 406 (2003).
[14] I. Ginzburg and D. d'Humières, Phys. Rev. E **68**, 066614 (2003).
[15] I. Ginzburg, Adv. Water Resour. **28**, 1196 (2005).
[16] C. P. Lowe, D. Frenkel, and A. J. Masters, J. Chem. Phys. **103**, 1582 (1995).
[17] X. D. Niu, C. Shu, Y. T. Chew, and Y. Peng, Phys. Lett. A **354**, 173 (2006).
[18] Y. Hu, H. Z. Yuan, S. Shu, X. D. Niu, and M. J. Li, Comput. Math. Appl. **68**, 140 (2014).
[19] H. Z. Yuan, X. D. Niu, S. Shu, M. J. Li, and H. Yamaguchi, Comput. Math. Appl. **67**, 1039 (2014).
[20] Y. Hu, D. C. Li, S. Shu, and X. D. Niu, Int. J. Heat Mass Transfer **81**, 591 (2015).
[21] Z. G. Feng and E. E. Michaelides, Comput. Fluids **38**, 370 (2009).
[22] Z. L. Guo, C. G. Zheng, and B. C. Shi, Phys. Rev. E **65**, 046308 (2002).
[23] C. S. Peskin, J. Comput. Phys. **25**, 220 (1977).
[24] G. Tryggvason, B. Bunner, A. Esmaeeli, D. Juric, N. Al-Rawahi, W. Tauber, J. Han, S. Nas, and Y. J. Jan, J. Comput. Phys. **169**, 708 (2001).
[25] J. H. Seo and R. Mittal, J. Comput. Phys. **230**, 7347 (2011).
[26] A. Caiazzo and M. Junk, Comput. Math. Appl. **55**, 1415 (2008).
[27] X. He and G. Doolen, J. Comput. Phys. **134**, 306 (1997).
[28] M. Rohde, J. J. Derksen, and H. E. A. Van den Akker, Phys. Rev. E **65**, 056701 (2002).
[29] X. L. Yang, X. Zhang, Z. L. Li, and G. W. He, J. Comput. Phys. **228**, 7821 (2009).
[30] J. Happel and H. Brener, *Low Reynolds number hydrodynamics* (Prentice-Hall, New York, 1965).
[31] D. Wan and S. Turek, Int. J. Numer. Meth. Fluids **51**, 531 (2006).
[32] R. Glowinski, T. W. Pan, T. I. Hesla, D. D. Joseph, and J. Périaux, J. Comput. Phys. **169**, 363 (2001).
[33] H. B. Li, X. Y. Lu, H. P. Fang, and Y. H. Qian, Phys. Rev. E **70**, 026701 (2004).
[34] H. H. Hu, N. A. Patankar, and M. Y. Zhu, J. Comput. Phys. **169**, 427 (2001).
[35] J. R. Clausen and C. K. Adiun, Int. J. Multiphase Flow **35**, 307 (2009).
[36] Z. Xia, K. W. Connington, S. Rapaka, P. Yue, J. J. Feng, and S. Chen, J. Fluid Mech. **625**, 249 (2009).
[37] A. T. Cate, C. H. Nieuwstad, J. J. Derksen, and H. E. A. Van den Akker, Phys. Fluids **14**, 4012 (2002).
[38] E. B. Saff and A. B. J. Kuijlaars, Math. Intell. **19**, 5 (1997).
[39] Z. G. Feng and E. E. Michaelides, J. Comput. Phys. **202**, 20 (2005).
[40] C.-C. Liao, Y.-W. Chang, C.-A. Lin, and J. M. McDonough, Comput. Fluids **39**, 152 (2010).
[41] K. Suzuki and T. Inamuro, Comput. Fluids **49**, 173 (2011).
[42] A. F. Fortes, D. D. Joseph, and T. S. Lundgren, J. Fluid Mech. **177**, 467 (1987).
[43] Z. G. Feng and E. Machaelides, J. Comput. Phys. **195**, 602 (2004).